

VISION-XL: High Definition Video Inverse Problem Solver using Latent Image Diffusion Models

Taesung Kwon Jong Chul Ye
 KAIST
 {star.kwon, jong.ye}@kaist.ac.kr

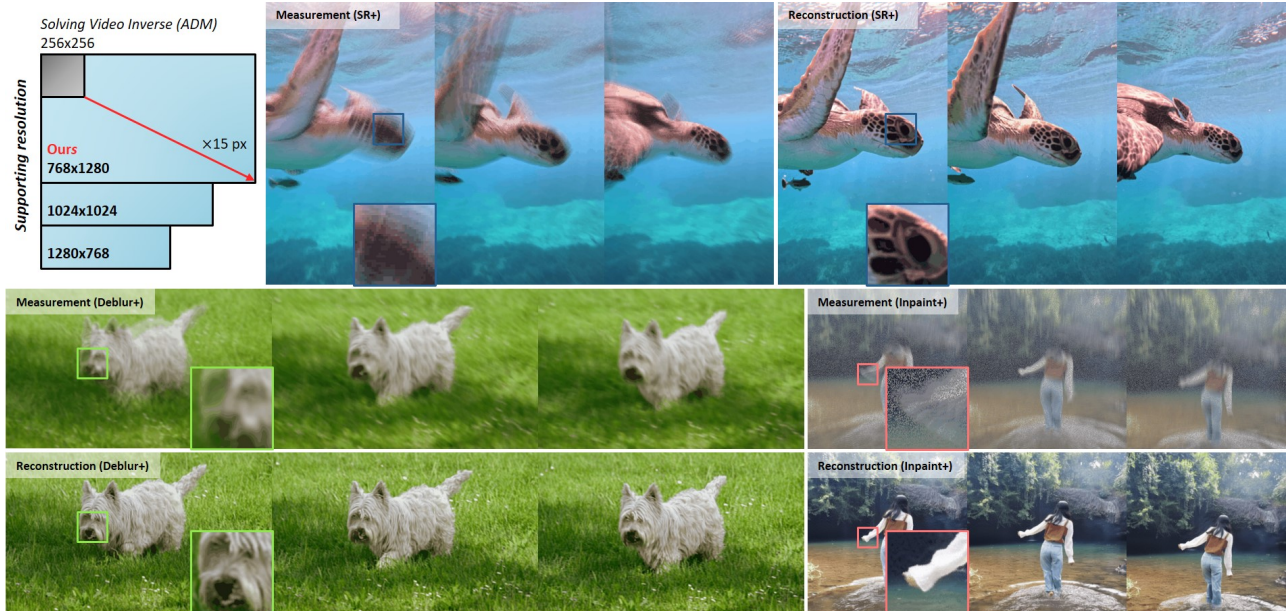


Figure 1. Representative video reconstruction results by VISION-XL for complex combinations of (top) frame averaging + super-resolution ($\times 4$), (bottom, left) frame averaging + deblur ($\sigma=3.0$), (bottom, right) frame averaging + inpaint (random, 50%).

Abstract

In this paper, we propose a novel framework for solving high-definition video inverse problems using latent image diffusion models. Building on recent advancements in spatio-temporal optimization for video inverse problems using image diffusion models, our approach leverages latent-space diffusion models to achieve enhanced video quality and resolution. To address the high computational demands of processing high-resolution frames, we introduce a pseudo-batch consistent sampling strategy, allowing efficient operation on a single GPU. Additionally, to improve temporal consistency, we present batch-consistent inversion, an initialization technique that incorporates informative latents from the measurement frame. By integrating with SDXL, our framework achieves state-of-the-art video reconstruction across a wide range of spatio-temporal inverse problems, including complex combinations of frame averaging and various spatial degradations, such as de-

blurring, super-resolution, and inpainting. Unlike previous methods, our approach supports multiple aspect ratios (landscape, vertical, and square) and delivers HD-resolution reconstructions (exceeding 1280×720) in under 2.5 minutes on a single NVIDIA 4090 GPU. Project page: <https://vision-xl.github.io/>.

1. Introduction

Diffusion models [6, 9, 10, 17, 19, 21, 23] have set a new benchmark in generative modeling, enabling the generation of high-quality samples. These models have become the foundation for advancements in various fields, such as controllable image editing [34], image personalization [8], synthetic data augmentation [24], and even reconstructing images from brain signals [14, 25].

Furthermore, diffusion model-based inverse problem solvers (DIS) [2, 4, 11, 22, 28, 30] address a variety of image restoration tasks, such as deblurring, super-resolution, inpainting, colorization, compressed sensing, and so on. A key feature of DIS is its plug-and-play capability, allowing

diffusion models to be applied flexibly across different inverse problems without requiring task-specific training or fine-tuning.

Recently, several extensions [5, 13, 33] from the DIS have been proposed to solve video inverse problems using image diffusion models. Naive application of image diffusion models to videos may break temporal consistency. To address this problem, these methods preserve temporal consistency by utilizing a batch-consistent sampling strategy [13] and applying optical flow guidance to warp either latent representations [33] or the noise prior [5].

Although these innovative approaches enable powerful image generative models [6, 17, 19] to solve video inverse problems with significantly reduced computational requirements, there is still room for improvement in these methods. Optical flow-based methods [5, 33] have reported a key limitation: their performance is highly dependent on the accuracy of the optical flow estimation module [26, 31]. This dependency becomes problematic when extreme degradations complicate the estimation process, restricting their applicability to a wider range of restoration tasks. Additionally, these methods require task-specific restoration modules [33] or fine-tuning of the diffusion model [5]. In this perspective, batch consistent sampling strategy [13] successfully addressed various spatio-temporal degradations without requiring task-specific training or fine-tuning. However, the reconstruction resolution is limited to 256×256 , as it utilizes the unconditional *pixel*-space diffusion model provided by ADM [6].

To overcome these limitations, here we propose a novel framework for solving high-definition video inverse problems using latent *image* diffusion models. Building on the success of solving spatio-temporal optimization problems within denoised batches [13] from *pixel*-space image diffusion models [6], we introduce a novel method that uses *latent*-space diffusion models [17] to solve spatio-temporal optimization problems. Specifically, to address the high computational demands of batch processing (e.g., 16-frame batches as used in [13]) with advanced latent diffusion models [17], we adopt a strategy called pseudo-batch consistent sampling. This approach helps manage the increased memory requirements, enabling the method to operate on a single GPU. Additionally, we introduce batch-consistent inversion, which allows us to initialize with informative latents from the measurement frame. This initialization enhances temporal consistency and improves the efficiency of solving spatio-temporal inverse problems.

By integrating these components, our framework achieves state-of-the-art video reconstruction performance using SDXL [17]. We name the method integrating these components as VISION-XL, short for **V**ideo **I**nverse-**S**olver using latent diffus**I**ON models (with stable diffusion **XL**). It supports various aspect ratios, including

landscape, vertical, and square formats. Thanks to its efficiency, our framework can reconstruct 25-frame videos at a resolution of 1280×768 (exceeding HD resolution) in under 2.5 minutes on a single NVIDIA 4090 GPU. Our contribution can be summarized as follows:

- We present a high-definition video inverse problem solver based on SDXL, which supports various aspect ratios and delivers state-of-the-art reconstruction performance.
- Within this novel framework, we introduce a pseudo-batch consistent sampling strategy and batch-consistent inversion, which enable more effective and efficient video reconstruction from various video inverse problems.

2. Related Work

Diffusion model-based inverse problem solvers (DIS). Diffusion models [9, 21, 23] attempt to model the data distribution $p_\theta(\mathbf{x})$ based on the Gaussian transitions. In the geometric view of diffusion models [1], the transitions are typically described as iterative manifold transitions $\mathcal{M}_t \rightarrow \mathcal{M}_{t-1}$, $t = T, \dots, 1$, moving from the noisy manifold \mathcal{M}_T to the clean manifold \mathcal{M}_0 .

Diffusion model-based inverse problem solvers (DIS) [2, 4, 11, 22, 28] aim to guide manifold transitions to sample from the posterior distribution $p_\theta(\mathbf{x}|\mathbf{y})$, which represents sampling \mathbf{x} from the measurement \mathbf{y} obtained from the forward model $\mathcal{A}(\mathbf{x})$. In Bayesian inference, the posterior distribution, $p_\theta(\mathbf{x}|\mathbf{y}) \propto p_\theta(\mathbf{x})p(\mathbf{y}|\mathbf{x})$ is decomposed into the likelihood $p(\mathbf{y}|\mathbf{x})$, representing the probability of observing \mathbf{y} given \mathbf{x} , and the prior data distribution $p_\theta(\mathbf{x})$. This decomposition enables posterior sampling by combining diffusion sampling with iterative guidance using the forward model \mathcal{A} and measurement \mathbf{y} . This approach provides sophisticated, precise solutions to complex inverse problems, leveraging the power and flexibility of diffusion models in practical applications, such as deblurring, super-resolution, inpainting, colorization, compressed sensing, and so on.

DIS using latent diffusion models (LDIS). Most DIS [2, 4, 11, 22, 28] use *pixel*-space diffusion models, which facilitate easy integration of the forward model \mathcal{A} and measurement \mathbf{y} , as both are defined in pixel space. Integrating forward models in latent space presents more challenges. *Latent*-space methods [3, 12, 20] calculate data consistency terms after decoding the denoised latent representation, then update these guidances within the latent space.

During this process, VAE mapping errors accumulate in iterative sampling, causing the representation to drift from the clean manifold \mathcal{M}_0 . Additionally, most latent diffusion models provide a text-conditioned prior distribution $p_\theta(\mathbf{x}|c_{\text{text}})$, which is challenging to implement in cases where text conditioning (c_{text}) is unavailable. As a result, *latent*-space methods prioritize two main goals: (i) managing text embeddings effectively and (ii) preserving the updated latent close to the clean manifold \mathcal{M}_0 .

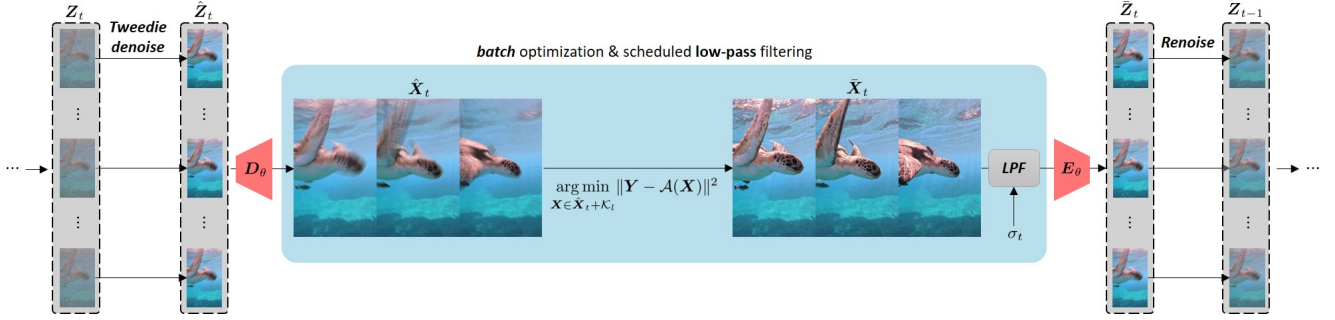


Figure 2. VISION-XL sampling process from initialization with batch-consistent inversion shown in Fig. 3.

For text embeddings, PSLD [20] uses only null-text, while TReg [12] and P2L [3] apply either null-text optimization or text optimization to enhance the reconstruction performance. To maintain the updated latent representation quality, the regularization term for aligning pixel and latent spaces is used to enforce latent feasibility [3, 12, 20].

Solving video inverse problems using DIS. Recently, several extensions [5, 13, 33] from DIS have been introduced to address video inverse problems. A straightforward application of image diffusion models to video, processing frames individually, often disrupts temporal consistency. These approaches maintain temporal coherence by employing a batch-consistent sampling strategy [13] and leveraging optical flow guidance to warp either latent representations [33] or the noise prior [5].

While these innovative approaches allow powerful image generative models [6, 17, 19] to address video inverse problems with reduced computational demands, there is still room for improvement. A key limitation of optical flow-based methods [5, 33] is their heavy reliance on the accuracy of the optical flow estimation module [26, 31]. This dependency becomes particularly problematic in scenarios involving severe degradations, which can hinder the estimation process and limit the methods’ applicability to broader restoration tasks. Moreover, these approaches often require task-specific restoration modules [33] or fine-tuning of the diffusion model [5].

In contrast, the batch-consistent sampling strategy [13] has demonstrated effectiveness in addressing various spatio-temporal degradations without the need for task-specific training or model fine-tuning. However, this method is limited by a reconstruction resolution of 256×256 , as it utilizes the unconditional *pixel*-space diffusion model provided by ADM [6]. In this work, we propose a framework that overcomes this resolution limitation by utilizing a *latent*-space diffusion model.

3. High Definition Video Inverse Solver Using Latent Diffusion Models

This section introduces a novel approach for reconstructing high-definition videos that include various spatio-temporal

degradations. The overall pipeline of the algorithm is illustrated in Fig. 2.

Consider the spatio-temporal degradation process is formulated as:

$$\mathbf{Y} = \mathcal{A}(\mathbf{X}) = \mathcal{A}([\mathbf{X}[1], \dots, \mathbf{X}[N]]) \quad (1)$$

where \mathbf{Y} denotes the measurement, $\mathbf{X}[n]$ denotes the n -th frame ground-truth frame, N is the number of video frames, and \mathcal{A} refers to the operator describing the spatio-temporal degradation process.

Our approach begins by inverting the initial measurement frame, denoted as $\mathbf{Y}[1]$, and replicating it N times to initialize the informative latents $\mathbf{Z}_\tau = [z_\tau \dots z_\tau]$, ensuring batch-wise consistency (Step 1). Next, we construct the corresponding denoised batch $\hat{\mathbf{X}}_\tau$ by sampling each latent in parallel using Tweedie’s formula [7], followed by decoding (Step 2). In Step 3, the corresponding denoised batch $\hat{\mathbf{X}}_\tau$ is further refined by applying l -step conjugate gradient (CG) optimization [4, 13] to enforce the data consistency from spatio-temporal degradation \mathcal{A} . In Step 4, we apply a scheduled low-pass filter to the updated batch $\bar{\mathbf{X}}_\tau$ inspired by the frequency-based analysis of spectral diffusion [32]. $\bar{\mathbf{X}}_\tau$ is then re-encoded into latent space to form $\bar{\mathbf{Z}}_\tau$. Finally, we obtain the one-step denoised latents $\mathbf{Z}_{\tau-1}$ by adding noise back to the encoded latents $\bar{\mathbf{Z}}_\tau$ (Step 5). In the following, we provide a detailed description of each of these steps.

Step 1: Initialize informative latents. One of our key insights is to initialize the informative latents by inverting the measurement frame and replicating it, thereby ensuring batch-wise consistent initialization (see Fig. 3). Although these latents cannot restore the ground-truth frames directly, inverted latent variables can inherit information from the measurement frame, providing good initializations [30]. Different from SVI [13] using replicated uninformative Gaussian prior $z_T \sim \mathcal{N}(0, I)$ as the initial sampling point, we replace the Gaussian prior with the replicated informative prior z_τ . Since the inversion time of a single measurement frame (under 2 seconds) is negligible compared to the sampling time, this approach not only offers a good initialization but also reduces the overall sampling time. The

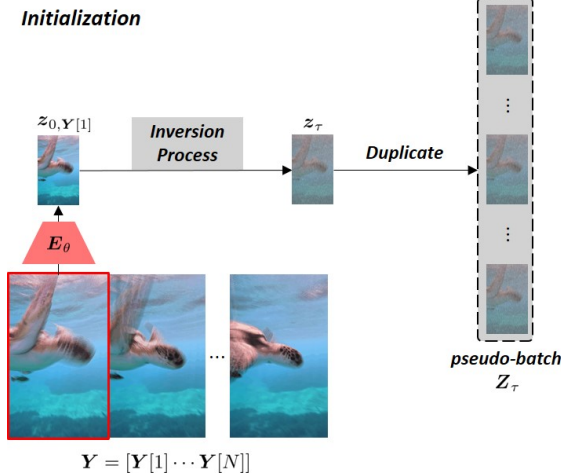


Figure 3. VISION-XL initialization using batch-consistent inversion of a measurement frame.

replicated informative prior Z_τ is represented as:

$$z_{Y[1]} = \mathbf{E}_\theta(Y[1]), z_\tau = \text{DDIM}^{-1}(z_{Y[1]}), Z_\tau := [z_\tau \cdots z_\tau]$$

where $\mathbf{E}_\theta(\cdot)$ and $\text{DDIM}^{-1}(\cdot)$ denotes encoding from pre-trained VAE and DDIM inversion of timestep τ , respectively.

Step 2: Denoised batch estimation. After initialization, we guide the sampling path to ensure the data consistency condition. At timestep $0 < t \leq \tau$, we sample denoise batch \hat{Z}_t from given latents $Z_t := [Z_t[1] \cdots Z_t[N]]$ by sampling each latent in parallel using Tweedie’s formula [7] and the latent diffusion model $\epsilon_\theta^{(t)}$. Unlike prior works [5, 13, 33], we sample latent frames in parallel, requiring memory for only a single frame during sampling. This enables the recent advanced latent diffusion model to operate in this framework without a frame limit. As a proof-of-concept, we conduct experiments on 25-frame videos.

Consider a parallel sampling of latent diffusion models along the temporal direction:

$$\mathcal{E}_\theta^{(t)}(Z_t) := [\epsilon_\theta^{(t)}(Z_t[1]) \cdots \epsilon_\theta^{(t)}(Z_t[N])]. \quad (2)$$

The denoised latents \hat{Z}_t are computed using Tweedie’s formula [7]:

$$\hat{Z}_t = \frac{1}{\sqrt{\bar{\alpha}_t}} \left(Z_t - \sqrt{1 - \bar{\alpha}_t} \mathcal{E}_\theta^{(t)}(Z_t) \right), \quad (3)$$

where $\bar{\alpha}_t$ is the noise schedule defined in the Gaussian process of diffusion models [9, 16]. Then denoised batch \hat{X}_t is decoded from the denoised latents \hat{Z}_t using VAE decoder D_θ :

$$\hat{X}_t = D_\theta(\hat{Z}_t) := [D_\theta(\hat{Z}_t[1]) \cdots D_\theta(\hat{Z}_t[N])]. \quad (4)$$

Step 3: DDS update in pixel-space. Inspired by batch-consistent sampling strategy [13], the latent diffusion models are initialized with the same informative latents using

batch-consistent inversion to ensure temporal consistency. Subsequently, the denoised batch \hat{X}_t is refined as a whole by applying the l -step CG optimization to enhance the data consistency from the spatio-temporal degradation \mathcal{A} . This can be formally represented by

$$\bar{X}_t := \arg \min_{X \in \hat{X}_t + \mathcal{K}_l} \|Y - \mathcal{A}(X)\|^2 \quad (5)$$

where \mathcal{K}_l denotes the l -dimensional Krylov subspace associated with the given inverse problem [4]. The multistep CG allows each temporal frame to be diversified, enhancing data consistency and achieving faster convergence without requiring memory-intensive gradient calculations [13]. In this work, we refer to this sampling scheme as pseudo-batch consistent sampling because we treat the parallel-sampled latents as a single batch for optimization.

Step 4: Low-pass filtered encoding. Recent frequency-based analyses of diffusion models [10, 32] suggest that optimal denoisers first recover low-frequency components in early denoising stages, with high-frequency details added progressively in later stages. Building on these findings, we observed that applying a scheduled low-pass filter to the updated batch \bar{X}_t in early stages yields more natural and refined results.

Based on the observation that the denoiser restores high-frequency details as the noise scale $\sqrt{1 - \bar{\alpha}_t}$ decreases, we set the filter width σ_t to be proportional to the noise scale [16], defined as $\sigma_t := \lambda \sqrt{1 - \bar{\alpha}_t}$, which goes to zero at $t \rightarrow 0$. After applying the low-pass filter h_{σ_t} , we re-encode \bar{X}_t into the latent space. Specifically, the re-encoded latents are given by:

$$\bar{X}_t \leftarrow \bar{X}_t * h_{\sigma_t}, \quad (6)$$

$$\bar{Z}_t = \mathbf{E}_\theta(\bar{X}_t) := [\mathbf{E}_\theta(\bar{X}_t[1]) \cdots \mathbf{E}_\theta(\bar{X}_t[N])], \quad (7)$$

where \mathbf{E}_θ denotes the VAE encoder.

Step 5: Renoising. After encoding, updated latents \bar{Z}_t are renoised as:

$$Z_{t-1} = \sqrt{\bar{\alpha}_{t-1}} \bar{Z}_t + \sqrt{1 - \bar{\alpha}_{t-1}} \mathcal{E}_t, \quad (8)$$

where \mathcal{E}_t is composed of batch-consistent noise [13] and deterministic noise [21].

In summary, the proposed method initializes informative latents and iteratively refines the decoded batch through multistep CG to meet spatio-temporal data consistency. We then apply low-pass filtered encoding to improve reconstruction quality. Extensive experimental results demonstrate that our method effectively addresses various spatio-temporal degradations, achieving state-of-the-art video reconstructions for high-definition videos and supporting a range of ratios previously unaddressed in other works. A geometric illustration of the sampling path evolution is shown in Fig. 4, and the complete algorithm is provided in Algorithm 1.

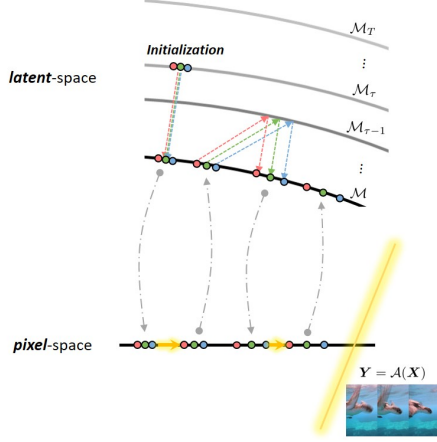


Figure 4. Geometric illustration of the sampling path evolution.

Algorithm 1 High-definition video inverse problem solver using latent diffusion models

Require: $\mathcal{E}_\theta^{(t)}, E_\theta, D_\theta, \mathbf{Y}, \mathcal{A}, \tau, l, \sigma_t, \{\alpha_t\}_{t=1}^T$

- 1: $z_{\mathbf{Y}[1]} \leftarrow E_\theta(\mathbf{Y}[1])$ ▷ **Step 1**
- 2: $z_\tau \leftarrow \text{DDIM}^{-1}(z_{\mathbf{Y}[1]})$
- 3: $\mathbf{Z}_\tau \leftarrow \text{Replicate}(z_\tau, N)$
- 4: **for** $t = \tau : 2$ **do**
- 5: $\hat{\mathbf{Z}}_t \leftarrow (\mathbf{Z}_t - \sqrt{1 - \bar{\alpha}_t} \mathcal{E}_\theta^{(t)}(\mathbf{Z}_t)) / \sqrt{\bar{\alpha}_t}$ ▷ **Step 2**
- 6: $\hat{\mathbf{X}}_t \leftarrow D_\theta(\hat{\mathbf{Z}}_t)$
- 7: $\bar{\mathbf{X}}_t := \arg \min_{\mathbf{X} \in \hat{\mathbf{X}}_t + \kappa_t} \|\mathbf{Y} - \mathcal{A}(\mathbf{X})\|^2$ ▷ **Step 3**
- 8: $\bar{\mathbf{X}}_t \leftarrow \bar{\mathbf{X}}_t * \mathbf{h}_{\sigma_t}$ ▷ **Step 4**
- 9: $\bar{\mathbf{Z}}_t = E_\theta(\bar{\mathbf{X}}_t)$
- 10: $\mathbf{Z}_{t-1} = \sqrt{\bar{\alpha}_{t-1}} \bar{\mathbf{Z}}_t + \sqrt{1 - \bar{\alpha}_{t-1}} \mathcal{E}_t$ ▷ **Step 5**
- 11: **end for**
- 12: $\mathbf{Z}_0 \leftarrow (\mathbf{Z}_1 - \sqrt{1 - \bar{\alpha}_1} \mathcal{E}_\theta^{(1)}(\mathbf{Z}_1)) / \sqrt{\bar{\alpha}_1}$
- 13: **return** \mathbf{Z}_0

4. Experimental Results

4.1. Experimental setup

Dataset. We used four high-resolution (with resolutions exceeding 1080p) video datasets for evaluation, sourced from the DAVIS dataset [18] and the Pexels dataset¹. A subset of 100 videos from the DAVIS dataset is resized to 768×1280 resolution and consists of 25 frames, originally provided in landscape orientation. The Pexels dataset is a large, open-source collection of high-resolution stock videos and images, widely used for creative and research purposes. For the Pexels subset, we collect a total of 120 videos: 45 in landscape orientation (Pexels (landscape)), 45 in vertical orientation (Pexels (vertical)), and 30 in square orientation (Pexels (square)). These subsets are resized to resolu-

tions of 768×1280 for landscape, 1280×768 for vertical, and 1024×1024 for square orientations, with each video consisting of 25 frames.

Inverse problems. We test our method on the following spatial degradations: **1) Deblur:** Gaussian deblurring from an image convolved with a 61×61 size Gaussian kernel with $\sigma=3.0$, **2) SR:** Super-resolution from $\times 4$ average pooling, **3) Inpaint:** Inpainting from 50% random masking. Furthermore, test our method on the following spatio-temporal degradations: **4) Deblur+:** Deblur + 7-frame averaging using temporal uniform blur kernel as used in [13], **5) SR+:** SR + 7-frame averaging, and **6) Inpaint+:** Inpaint + 7-frame averaging.

Baseline comparison. The primary objective of this study is to improve the performance of video inverse problem solvers through latent image diffusion models. Thus, our evaluation primarily compares video inverse problem solvers using image diffusion models. As a recently emerging field, only a few methods are available: SVI [13], DiffIR2VR [33], and Warped Diffusion [5]. Notably, DiffIR2VR and Warped Diffusion cannot address spatio-temporal degradations, and DiffIR2VR only supports SR among the inverse problems we address in this paper. We conducted comparisons with SVI and DiffIR2VR but excluded Warped Diffusion, as it is not currently open-source. SVI officially supports a resolution of 256×256, while DiffIR2VR supports 480×854. To ensure fair comparisons with identical resolutions, we used patch reconstruction. Additionally, we included a comparison with the classical optimization method ADMM-TV, following the protocol established by SVI [13].

For quantitative comparison, we focus on two widely used standard metrics: peak signal-to-noise ratio (PSNR) and structural similarity index (SSIM)[29]. Additionally, we evaluate two perceptual metrics: Learned Perceptual Image Patch Similarity (LPIPS)[35] and Fréchet Video Distance (FVD) [27]. For computing FVD, the videos are resized to 224×224 resolution and we follow the protocol from the open-source project².

Implementation details. While our method is applicable to general latent diffusion models, we use Stable Diffusion XL 1.0 (SDXL) [17]—the current state-of-the-art text-to-image diffusion model—as a proof of concept in this paper. For all experiments, we employ $T = 25$, $\tau = 0.3T$, $\lambda = 2$, and $l = 10$. These optimal values are obtained through extensive ablation studies and the results are described in Sec. 4.3. To reduce undesired guidance from the text condition c_{text} , we use a null-text condition, c_\emptyset . All experiments were done on a single NVIDIA 4090 GPU.

¹<https://www.pexels.com/>

²https://github.com/JunyaoHu/common_metrics_on_video_quality

| Task | Method | DAVIS | | | | Pexels (landscape) | | | | Pexels (vertical) | | | | Pexels (square) | | | |
|----------|----------------|--------------|--------------|--------------|--------------|--------------------|--------------|--------------|--------------|-------------------|--------------|--------------|--------------|-----------------|--------------|--------------|--------------|
| | | FVD↓ | LPIPS↓ | PSNR↑ | SSIM↑ | FVD↓ | LPIPS↓ | PSNR↑ | SSIM↑ | FVD↓ | LPIPS↓ | PSNR↑ | SSIM↑ | FVD↓ | LPIPS↓ | PSNR↑ | SSIM↑ |
| Deblur+ | ADMM-TV | 1893 | 0.361 | 23.76 | 0.720 | 1038 | 0.262 | 29.31 | 0.830 | <u>1169</u> | 0.241 | 29.85 | 0.845 | 1068 | 0.223 | 29.74 | 0.850 |
| | SVI [13] | <u>621.5</u> | <u>0.175</u> | <u>31.27</u> | <u>0.881</u> | <u>815.2</u> | <u>0.197</u> | <u>31.62</u> | <u>0.886</u> | 1237 | <u>0.193</u> | <u>31.57</u> | <u>0.889</u> | <u>789.7</u> | <u>0.150</u> | <u>32.63</u> | <u>0.905</u> |
| | DiffIR2VR [33] | - | - | - | - | - | - | - | - | - | - | - | - | - | - | - | - |
| | Ours | 142.6 | 0.027 | 34.96 | 0.958 | 90.86 | 0.015 | 38.16 | 0.970 | 97.57 | 0.009 | 38.93 | 0.977 | 94.33 | 0.015 | 39.01 | 0.968 |
| SR+ | ADMM-TV | 1705 | 0.325 | 23.83 | 0.724 | 913.8 | 0.235 | 28.86 | 0.821 | 1014 | 0.218 | 29.20 | 0.835 | 908.4 | 0.203 | 29.12 | 0.839 |
| | SVI [13] | <u>213.5</u> | <u>0.096</u> | <u>32.49</u> | <u>0.895</u> | <u>375.1</u> | <u>0.120</u> | <u>33.23</u> | <u>0.888</u> | <u>549.6</u> | <u>0.117</u> | <u>32.95</u> | <u>0.887</u> | <u>308.3</u> | <u>0.085</u> | <u>34.52</u> | <u>0.903</u> |
| | DiffIR2VR [33] | - | - | - | - | - | - | - | - | - | - | - | - | - | - | - | - |
| | Ours | 81.54 | 0.018 | 35.87 | 0.965 | 67.42 | 0.017 | 37.84 | 0.965 | 66.46 | 0.014 | 38.47 | 0.971 | 67.86 | 0.017 | 38.69 | 0.961 |
| Inpaint+ | ADMM-TV | 1955 | 0.315 | 23.47 | 0.737 | 930.8 | 0.174 | 30.34 | 0.869 | 928.9 | 0.155 | 30.92 | 0.884 | 881.4 | 0.158 | 30.63 | 0.885 |
| | SVI [13] | 107.6 | 0.025 | 37.47 | 0.966 | <u>269.0</u> | <u>0.036</u> | 36.80 | 0.959 | <u>425.3</u> | <u>0.033</u> | 37.18 | <u>0.960</u> | <u>205.5</u> | <u>0.027</u> | 38.77 | 0.972 |
| | DiffIR2VR [33] | - | - | - | - | - | - | - | - | - | - | - | - | - | - | - | - |
| | Ours | <u>166.8</u> | <u>0.027</u> | <u>34.96</u> | <u>0.958</u> | 113.2 | 0.026 | <u>35.11</u> | <u>0.956</u> | 123.9 | 0.020 | <u>35.96</u> | 0.964 | 120.0 | 0.026 | <u>36.06</u> | <u>0.953</u> |
| Deblur | ADMM-TV | 519.5 | 0.181 | 32.48 | 0.894 | 457.7 | 0.181 | 34.70 | 0.905 | 533.4 | 0.172 | 34.44 | 0.910 | 450.8 | 0.139 | 35.82 | 0.920 |
| | SVI [13] | <u>90.84</u> | <u>0.088</u> | <u>37.17</u> | <u>0.954</u> | <u>139.7</u> | <u>0.113</u> | <u>38.08</u> | <u>0.947</u> | <u>144.9</u> | <u>0.108</u> | <u>37.96</u> | <u>0.949</u> | <u>107.0</u> | <u>0.075</u> | <u>39.89</u> | <u>0.957</u> |
| | DiffIR2VR [33] | - | - | - | - | - | - | - | - | - | - | - | - | - | - | - | - |
| | Ours | 13.25 | 0.004 | 40.79 | 0.988 | 13.30 | 0.005 | 41.08 | 0.984 | 13.20 | 0.004 | 41.66 | 0.985 | 11.88 | 0.004 | 41.83 | 0.978 |
| SR | ADMM-TV | 414.5 | 0.164 | 30.52 | 0.860 | 338.8 | 0.168 | 32.73 | 0.867 | 425.8 | 0.161 | 32.19 | 0.882 | 375.3 | 0.138 | 33.30 | 0.887 |
| | SVI [13] | <u>166.1</u> | <u>0.089</u> | <u>32.88</u> | <u>0.899</u> | <u>188.6</u> | <u>0.106</u> | <u>34.26</u> | <u>0.894</u> | <u>205.6</u> | <u>0.104</u> | <u>33.79</u> | <u>0.893</u> | <u>159.7</u> | <u>0.077</u> | <u>35.38</u> | <u>0.907</u> |
| | DiffIR2VR [33] | 212.0 | 0.061 | 30.51 | 0.899 | 263.4 | 0.072 | 31.66 | 0.898 | 301.3 | 0.056 | 31.31 | 0.907 | 355.9 | 0.093 | 31.59 | 0.879 |
| | Ours | 16.34 | 0.009 | 38.72 | 0.983 | 16.05 | 0.008 | 39.73 | 0.980 | 15.70 | 0.005 | 40.80 | 0.983 | 13.00 | 0.005 | 40.93 | 0.977 |
| Inpaint | ADMM-TV | 288.0 | 0.136 | 32.26 | 0.921 | 193.4 | 0.082 | 36.18 | 0.952 | 177.5 | 0.074 | 36.39 | 0.959 | 182.9 | 0.076 | 36.80 | 0.960 |
| | SVI [13] | 42.17 | 0.015 | 39.87 | 0.977 | 58.26 | 0.020 | 39.86 | 0.970 | 62.80 | 0.019 | 39.95 | 0.969 | 38.66 | 0.015 | 42.10 | 0.980 |
| | DiffIR2VR [33] | - | - | - | - | - | - | - | - | - | - | - | - | - | - | - | - |
| | Ours | <u>73.85</u> | <u>0.022</u> | <u>35.27</u> | <u>0.968</u> | <u>77.03</u> | <u>0.023</u> | <u>35.48</u> | <u>0.959</u> | <u>69.72</u> | 0.019 | <u>36.05</u> | <u>0.964</u> | <u>67.01</u> | <u>0.021</u> | <u>36.28</u> | <u>0.955</u> |

Table 1. Quantitative evaluation (FVD, LPIPS, PSNR, SSIM) of solving spatio-temporal inverse problems across DAVIS, Pexels dataset with multiple aspect ratios (landscape, vertical, square).

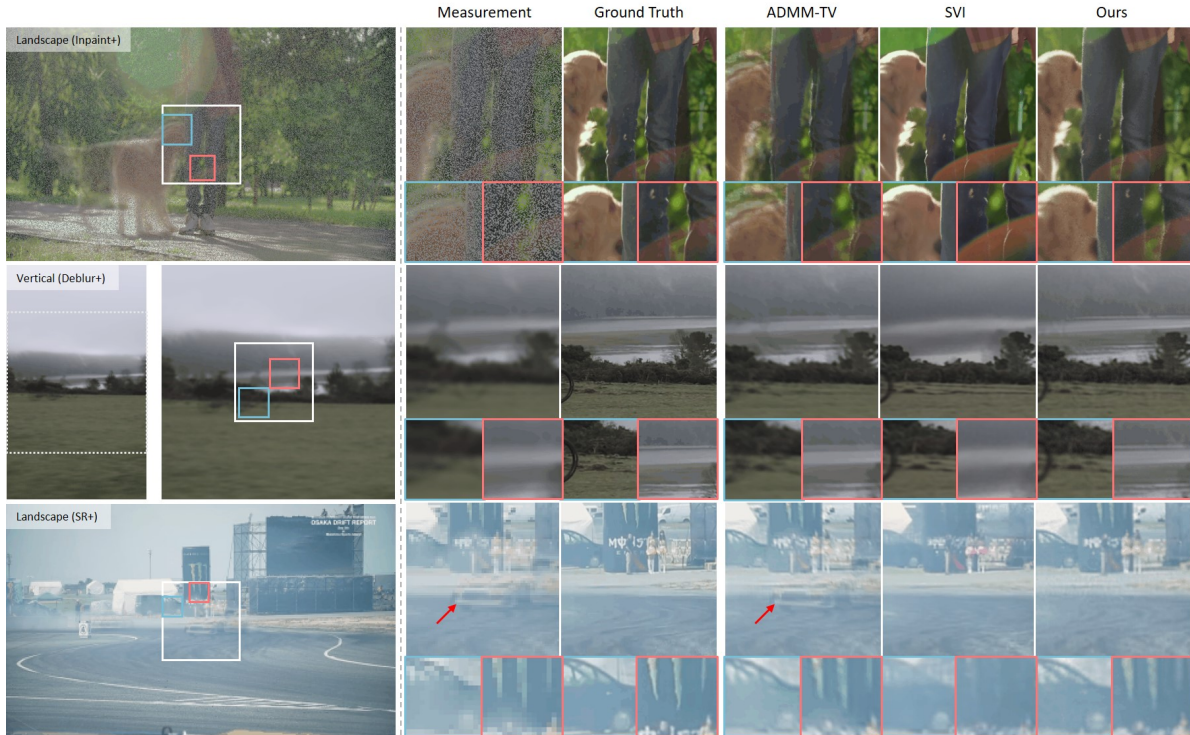


Figure 5. Qualitative evaluation of solving spatio-temporal inverse problems across DAVIS, Pexels dataset with multiple aspect ratios (landscape, vertical, square).

4.2. Results

Table 1 presents the quantitative comparisons across various spatio-temporal inverse problems. The proposed method

consistently outperforms the baseline approaches in most metrics, particularly for solving spatio-temporal degradations. Notably, we observe a significant decrease in FVD,

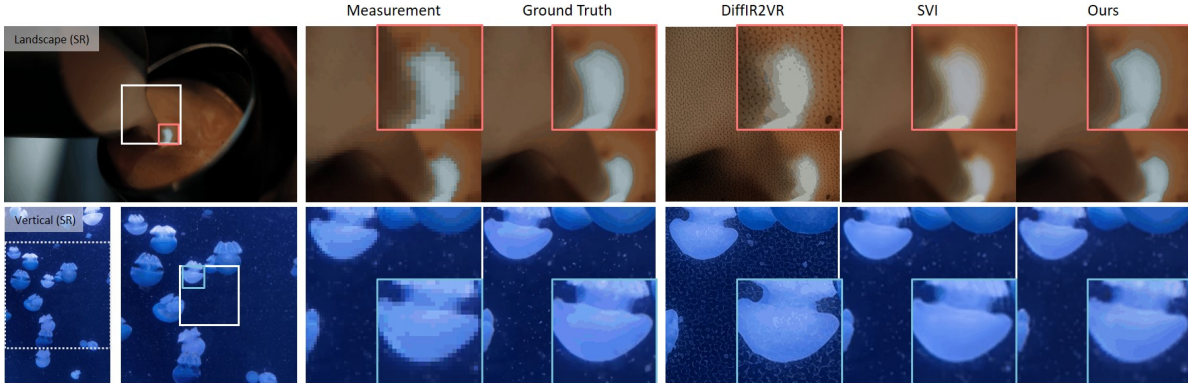


Figure 6. Qualitative evaluation of solving SR($\times 4$) across multiple aspect ratios (landscape, vertical).

| Method | Resolution | Time / patch [s] | Time [min] | Memory (GB) |
|----------------|-------------------|------------------|------------|-------------|
| SVI [13] | 256 \times 256 | 60 | 15 | 18.5 |
| DiffIR2VR [33] | 480 \times 854 | 70 | 4.7 | 13.6 |
| Ours | 768 \times 1280 | 150 | 2.5 | 12.7 |

Table 2. Comparison on supporting resolution, total sampling time, and memory efficiency of solving video inverse problems of 25-frame 768 \times 1280 resolution.

indicating superior video perceptual quality compared to the runner-up across all datasets. This improvement is also evident in the qualitative results shown in Fig. 5. While SVI [13] performs well on spatio-temporal degradations, it often struggles to maintain temporal consistency, resulting in issues such as incorrect frame intensity restoration (first row) and loss of background details (second and third rows). This suggests that batch-consistent noise initialization [13], as further examined in our ablation study in Table 3, may be insufficient to fully preserve temporal consistency. Additionally, its limited supported resolution necessitates patch reconstruction, which can introduce patch-wise inconsistency and contribute to performance degradation. The classical optimization method, ADMM-TV, performs well in reconstructing static backgrounds or stationary objects but struggles to reconstruct dynamic scenes or objects, as shown in Fig. 5, which is reflected in its lower metrics. In comparison with DiffIR2VR [33] on the SR task (Fig. 6), we observe that DiffIR2VR often produces unwanted artifacts in backgrounds or over-generates details of objects. These issues likely stem from challenges in optical flow estimation from the measurement. While these baseline methods encounter various challenges across different inverse problems, our method demonstrates stable, high-quality reconstruction without the need for patch reconstruction, as evidenced by the overall results. Further comparisons of supported resolution, total sampling time, and memory consumption are shown in Table 2. As shown in the table, our method achieves the highest efficiency in both sampling time and memory usage. Ad-

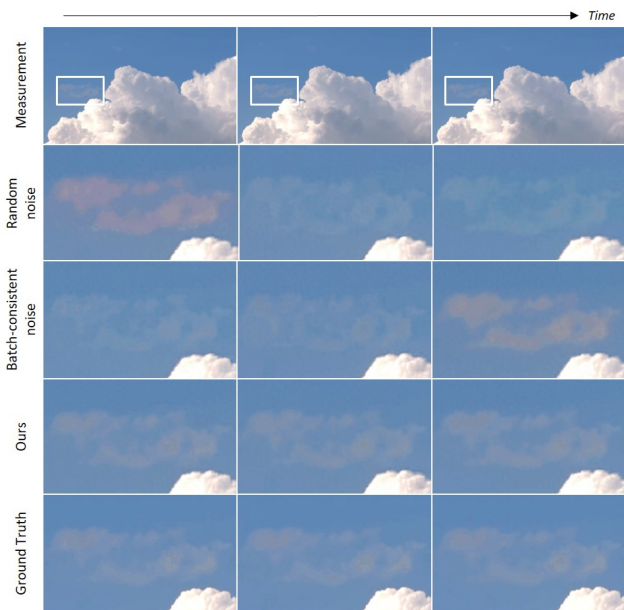


Figure 7. Ablation study on the effect of the initializations.

ditional visualizations, including reconstruction results for deblurring, inpainting, and other tasks, are available in video format for further evaluation on the following page: <https://vision-xl.github.io/supple/>.

4.3. Ablation studies

In this subsection, we present an in-depth analysis of the key components in our method.

| Initialization | Time [min] | FVD \downarrow | LPIPS \downarrow | PSNR \uparrow | SSIM \uparrow |
|--|------------|------------------|--------------------|-----------------|-----------------|
| Random noise | 8.3 | 1015 | 0.031 | 34.28 | 0.954 |
| Batch-consistent noise [13] | 8.3 | 661.3 | 0.024 | 36.04 | 0.961 |
| Batch-consistent inversion ($\tau: 0.15T$) | 1.3 | 106.5 | 0.020 | 37.12 | 0.962 |
| Batch-consistent inversion ($\tau: 0.30T$) | 2.5 | 83.35 | 0.017 | 37.86 | 0.966 |
| Batch-consistent inversion ($\tau: 0.45T$) | 3.8 | 176.7 | 0.018 | 37.70 | 0.965 |

Table 3. Ablation study on the effect of the initializations.

Effect of initialization (in Step 1). In Table 3, we con-

duct an ablation study using the Pexels (landscape) dataset to see the effect of batch-consistent inversion for initialization. From the table, we confirm that batch-consistent inversion effectively extracts informative latents to reconstruct video evidenced by about 1.8dB PSNR increase and 3.5dB PSNR increase compared with batch-consistent noise initialization used in SVI [13] and random noise initialization, respectively. Notably, batch-consistent inversion achieves $\times 8$ lower FVD compared to the runner-up which indicates a significant improvement in temporal consistency. It is also evident in the visualization of the ablation study shown in Fig. 7. The reconstruction results from random noise and batch-consistent noise initialization fail to reconstruct the color of the cloud and are temporally inconsistent. In contrast, our method successfully reconstructs the color of the cloud and temporally consistent results. Furthermore, thanks to the fast inversion of a single frame (e.g., within two seconds for τ : $0.30T$), batch-consistent inversion efficiently reduces sampling time by about $\times 3$ compared to the full samplings. The multi-step CG guidance and batch-consistent inversion synergistically combine to enable high-definition video reconstruction in under 2.5 minutes on a single NVIDIA 4090 GPU.

| Update step l | FVD \downarrow | LPIPS \downarrow | PSNR \uparrow | SSIM \uparrow |
|-----------------|------------------|--------------------|-----------------|-----------------|
| 1 | 906.5 | 0.096 | 31.74 | <u>0.905</u> |
| 5 | <u>123.6</u> | 0.017 | <u>37.13</u> | 0.966 |
| 10 | 83.35 | 0.017 | 37.86 | 0.966 |
| 20 | 278.5 | <u>0.076</u> | 34.74 | 0.900 |

Table 4. Ablation study on the effect of l .

Effect of optimization step l (in Step 3). In Table 4, we present an ablation study on the effect of the CG update step l . The table confirms that the CG update is essential for enhancing data consistency. We found that at least 5 iterations of CG updates yield satisfactory results, with 10 iterations producing the best outcomes.

| LPF λ | FVD \downarrow | LPIPS \downarrow | PSNR \uparrow | SSIM \uparrow |
|---------------|------------------|--------------------|-----------------|-----------------|
| No LPF | 103.4 | 0.017 | 37.57 | 0.965 |
| 1 | 83.08 | 0.016 | 37.85 | <u>0.966</u> |
| $\sqrt{2}$ | 83.35 | <u>0.017</u> | <u>37.86</u> | <u>0.966</u> |
| 2 | 79.61 | 0.018 | 37.83 | <u>0.966</u> |
| $2\sqrt{2}$ | <u>82.04</u> | 0.020 | 37.92 | 0.967 |

Table 5. Ablation study on the effect of LPF λ .

Effect of LPF λ (in Step 4). Table 5 presents an ablation study on the effect of low-pass filtering. The results confirm that low-pass filtering enhances the reconstruction quality as evidenced by all metrics. Specifically, low-pass filtering results in approximately a 20-point decrease in FVD and a 0.3dB increase in PSNR compared to the absence of low-pass filtering. This improvement is also evident in the visualizations in Fig. 8. In the second row of the figure, undesired artifacts appear when low-pass filtering is not ap-

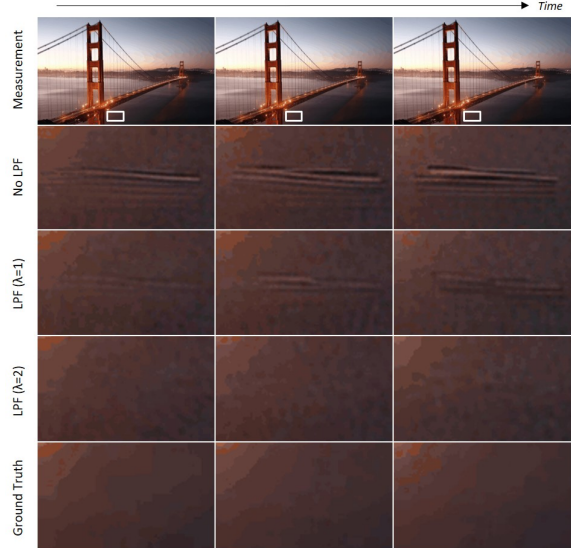


Figure 8. Ablation study on the effect of low-pass filtering.

plied. In contrast, as shown in the third and fourth rows, these artifacts are effectively removed as the parameter λ increases. From a frequency-based perspective, we believe that low-pass filtering effectively guides the updated latents to remain within the desired denoised manifold, \mathcal{M}_0 , and helps to mitigate error accumulation from the VAE.

5. Conclusion

In this paper, we proposed a novel framework for addressing high-definition video inverse problems using latent diffusion models that introduce two new strategies. First, a pseudo-batch consistent sampling strategy to manage intensive batch memory consumption with advanced latent diffusion models (e.g., SDXL). To acquire a denoised batch, we conduct parallel sampling of each latents rather than batch sampling to efficiently manage the high memory consumption of advanced latent diffusion models. Second, a batch-consistent inversion for leveraging informative latent as initialization is proposed. We confirmed that batch-consistent inversion significantly improves reconstruction performance in both traditional and perceptual quality metrics. Leveraging the powerful SDXL, our method achieves state-of-the-art performance across diverse spatio-temporal inverse problems, including challenging tasks such as the combination of frame averaging with deblurring, super-resolution, and inpainting. Importantly, our method supports multiple aspect ratios (landscape, vertical, and square), making it versatile for different video formats and delivering HD reconstructions in under 2.5 minutes on a single NVIDIA 4090 GPU. Overall, our framework not only enhances video reconstruction quality but also sets new standards for efficiency and flexibility in solving high-definition video inverse problems.

References

- [1] Hyungjin Chung, Byeongsu Sim, Dohoon Ryu, and Jong Chul Ye. Improving diffusion models for inverse problems using manifold constraints. *Advances in Neural Information Processing Systems*, 35:25683–25696, 2022. 2
- [2] Hyungjin Chung, Jeongsol Kim, Michael Thompson McCann, Marc Louis Klasky, and Jong Chul Ye. Diffusion posterior sampling for general noisy inverse problems. In *International Conference on Learning Representations*, 2023. 1, 2
- [3] Hyungjin Chung, Jong Chul Ye, Peyman Milanfar, and Mauricio Delbracio. Prompt-tuning latent diffusion models for inverse problems. *arXiv preprint arXiv:2310.01110*, 2023. 2, 3
- [4] Hyungjin Chung, Suhyeon Lee, and Jong Chul Ye. Decomposed diffusion sampler for accelerating large-scale inverse problems. In *The Twelfth International Conference on Learning Representations*, 2024. 1, 2, 3, 4
- [5] Giannis Daras, Weili Nie, Karsten Kreis, Alex Dimakis, Morteza Mardani, Nikola Borislavov Kovachki, and Arash Vahdat. Warped diffusion: Solving video inverse problems with image diffusion models. *arXiv preprint arXiv:2410.16152*, 2024. 2, 3, 4, 5
- [6] Prafulla Dhariwal and Alexander Nichol. Diffusion models beat gans on image synthesis. *Advances in neural information processing systems*, 34:8780–8794, 2021. 1, 2, 3
- [7] Bradley Efron. Tweedie’s formula and selection bias. *Journal of the American Statistical Association*, 106(496):1602–1614, 2011. 3, 4
- [8] Rinon Gal, Yuval Alaluf, Yuval Atzmon, Or Patashnik, Amit H Bermano, Gal Chechik, and Daniel Cohen-Or. An image is worth one word: Personalizing text-to-image generation using textual inversion. *arXiv preprint arXiv:2208.01618*, 2022. 1
- [9] Jonathan Ho, Ajay Jain, and Pieter Abbeel. Denoising diffusion probabilistic models. *Advances in Neural Information Processing Systems*, 33:6840–6851, 2020. 1, 2, 4
- [10] Tero Karras, Miika Aittala, Timo Aila, and Samuli Laine. Elucidating the design space of diffusion-based generative models. *Advances in neural information processing systems*, 35:26565–26577, 2022. 1, 4
- [11] Bahjat Kavar, Michael Elad, Stefano Ermon, and Jiaming Song. Denoising diffusion restoration models. *Advances in Neural Information Processing Systems*, 35:23593–23606, 2022. 1, 2
- [12] Jeongsol Kim, Geon Yeong Park, Hyungjin Chung, and Jong Chul Ye. Regularization by texts for latent diffusion inverse solvers. *arXiv preprint arXiv:2311.15658*, 2023. 2, 3
- [13] Taesung Kwon and Jong Chul Ye. Solving video inverse problems using image diffusion models. *arXiv preprint arXiv:2409.02574*, 2024. 2, 3, 4, 5, 6, 7, 8, 1
- [14] Dongyang Li, Chen Wei, Shiyang Li, Jiachen Zou, and Quanying Liu. Visual decoding and reconstruction via eeg embeddings with guided diffusion. *arXiv preprint arXiv:2403.07721*, 2024. 1
- [15] Seungjun Nah, Tae Hyun Kim, and Kyoung Mu Lee. Deep multi-scale convolutional neural network for dynamic scene deblurring. In *Proceedings of the IEEE conference on computer vision and pattern recognition*, pages 3883–3891, 2017. 1, 2
- [16] Alexander Quinn Nichol and Prafulla Dhariwal. Improved denoising diffusion probabilistic models. In *International Conference on Machine Learning*, pages 8162–8171. PMLR, 2021. 4
- [17] Dustin Podell, Zion English, Kyle Lacey, Andreas Blattmann, Tim Dockhorn, Jonas Müller, Joe Penna, and Robin Rombach. Sdxl: Improving latent diffusion models for high-resolution image synthesis. *arXiv preprint arXiv:2307.01952*, 2023. 1, 2, 3, 5
- [18] Jordi Pont-Tuset, Federico Perazzi, Sergi Caelles, Pablo Arbeláez, Alex Sorkine-Hornung, and Luc Van Gool. The 2017 davis challenge on video object segmentation. *arXiv preprint arXiv:1704.00675*, 2017. 5
- [19] Robin Rombach, Andreas Blattmann, Dominik Lorenz, Patrick Esser, and Björn Ommer. High-resolution image synthesis with latent diffusion models. In *Proceedings of the IEEE/CVF conference on computer vision and pattern recognition*, pages 10684–10695, 2022. 1, 2, 3
- [20] Litu Rout, Negin Raouf, Giannis Daras, Constantine Caramanis, Alex Dimakis, and Sanjay Shakkottai. Solving linear inverse problems provably via posterior sampling with latent diffusion models. *Advances in Neural Information Processing Systems*, 36, 2024. 2, 3
- [21] Jiaming Song, Chenlin Meng, and Stefano Ermon. Denoising diffusion implicit models. In *International Conference on Learning Representations*, 2021. 1, 2, 4
- [22] Jiaming Song, Arash Vahdat, Morteza Mardani, and Jan Kautz. Pseudoinverse-guided diffusion models for inverse problems. In *International Conference on Learning Representations*, 2023. 1, 2
- [23] Yang Song, Jascha Sohl-Dickstein, Diederik P Kingma, Abhishek Kumar, Stefano Ermon, and Ben Poole. Score-based generative modeling through stochastic differential equations. In *International Conference on Learning Representations*, 2020. 1, 2
- [24] Andreas Stöckl. Evaluating a synthetic image dataset generated with stable diffusion. In *International Congress on Information and Communication Technology*, pages 805–818. Springer, 2023. 1
- [25] Yu Takagi and Shinji Nishimoto. High-resolution image reconstruction with latent diffusion models from human brain activity. In *Proceedings of the IEEE/CVF Conference on Computer Vision and Pattern Recognition*, pages 14453–14463, 2023. 1
- [26] Zachary Teed and Jia Deng. Raft: Recurrent all-pairs field transforms for optical flow. In *Computer Vision—ECCV 2020: 16th European Conference, Glasgow, UK, August 23–28, 2020, Proceedings, Part II 16*, pages 402–419. Springer, 2020. 2, 3
- [27] Thomas Unterthiner, Sjoerd van Steenkiste, Karol Kurach, Raphaël Marinier, Marcin Michalski, and Sylvain Gelly. Fvd: A new metric for video generation. 2019. 5

- [28] Yinhuai Wang, Jiwen Yu, and Jian Zhang. Zero-shot image restoration using denoising diffusion null-space model. In *The Eleventh International Conference on Learning Representations*, 2023. [1](#), [2](#)
- [29] Zhou Wang, Alan C Bovik, Hamid R Sheikh, and Eero P Simoncelli. Image quality assessment: from error visibility to structural similarity. *IEEE transactions on image processing*, 13(4):600–612, 2004. [5](#)
- [30] Jie Xiao, Ruili Feng, Han Zhang, Zhiheng Liu, Zhantao Yang, Yurui Zhu, Xueyang Fu, Kai Zhu, Yu Liu, and Zheng-Jun Zha. Dreamclean: Restoring clean image using deep diffusion prior. In *The Twelfth International Conference on Learning Representations*, 2024. [1](#), [3](#)
- [31] Haofei Xu, Jing Zhang, Jianfei Cai, Hamid Rezaatofghi, and Dacheng Tao. Gmflow: Learning optical flow via global matching. In *Proceedings of the IEEE/CVF conference on computer vision and pattern recognition*, pages 8121–8130, 2022. [2](#), [3](#)
- [32] Xingyi Yang, Daquan Zhou, Jiashi Feng, and Xinchao Wang. Diffusion probabilistic model made slim. In *Proceedings of the IEEE/CVF Conference on computer vision and pattern recognition*, pages 22552–22562, 2023. [3](#), [4](#)
- [33] Chang-Han Yeh, Chin-Yang Lin, Zhixiang Wang, Chi-Wei Hsiao, Ting-Hsuan Chen, and Yu-Lun Liu. Diffir2vr-zero: Zero-shot video restoration with diffusion-based image restoration models. *arXiv preprint arXiv:2407.01519*, 2024. [2](#), [3](#), [4](#), [5](#), [6](#), [7](#), [1](#)
- [34] Lvmin Zhang, Anyi Rao, and Maneesh Agrawala. Adding conditional control to text-to-image diffusion models. In *Proceedings of the IEEE/CVF International Conference on Computer Vision*, pages 3836–3847, 2023. [1](#)
- [35] Richard Zhang, Phillip Isola, Alexei A Efros, Eli Shechtman, and Oliver Wang. The unreasonable effectiveness of deep features as a perceptual metric. In *CVPR*, 2018. [5](#)

VISION-XL: High Definition Video Inverse Problem Solver using Latent Image Diffusion Models

Supplementary Material

6. Experimental details

6.1. Implementation of Comparative Methods

SVI [13]. For SVI, we use the official implementation³. Specifically, we utilize the same pre-trained image diffusion model, the unconditional ADM [6]. Following the protocol described in [13], we set the parameters as $l = 5$ and $\eta = 0.8$ with 100 NFE sampling. Since SVI officially supports a resolution of 256×256 , we applied patch-based reconstruction to ensure fair comparisons at identical resolutions.

DiffIR2VR [33]. For DiffIR2VR, we use the official implementation⁴. Specifically, we employ the same pre-trained image diffusion model, Stable Diffusion 2.1 [19]. DiffIR2VR is designed to support only super-resolution (SR) within the scope of our inverse problem. Therefore, we conducted SR experiments exclusively. Following the protocol in [33], we set the upscale factor to 4 and the CFG scale factor to 4, with 50 NFE sampling. DiffIR2VR officially supports resolutions of 480×854 . To ensure fair comparisons across resolutions, we applied patch-based reconstruction. For different aspect ratios, we set the resolution to 480×854 for landscape orientation, 854×480 for vertical orientation, and 512×512 for square.

ADMM-TV. Following the protocol in [13], we optimize the following objective:

$$\mathbf{X}^* = \operatorname{argmin}_{\mathbf{X}} \frac{1}{2} \|\mathbf{A}\mathbf{X} - \mathbf{Y}\|_2^2 + \lambda \|\mathbf{D}\mathbf{X}\|_1, \quad (9)$$

where $\mathbf{D} = [\mathbf{D}_t, \mathbf{D}_h, \mathbf{D}_w]$ corresponds to the classical Total Variation (TV) regularization. Here, t , h , and w represent temporal, height, and width directions, respectively. The outer iterations of ADMM were set to 30, and the inner iterations of conjugate gradient (CG) were set to 20, consistent with the settings in [13]. The parameters were set to $(\rho, \lambda) = (1, 0.001)$. The initial value of \mathbf{X} was set to zero.

7. Extension to blind video inverse problems

Our method can be extended to address blind video inverse problems, such as blind video deblurring, demonstrated using the widely-used GoPro dataset [15]. Here, we provide an example application of our method to blind video deblurring, showing its potential as a general framework for solving blind video inverse problems.

³<https://github.com/solving-video-inverse/codes>

⁴<https://github.com/jimmymcv07/DiffIR2VR-Zero>

Algorithm 2 Ours (blind) - Blind video deconvolution

Require: $\mathcal{E}_\theta^{(t)}, \mathbf{E}_\theta, \mathbf{D}_\theta, \mathbf{Y}, \tau, l, \sigma_t, \{\alpha_t\}_{t=1}^T, f_\phi$

- 1: $\mathbf{X}_{\text{pre}} \leftarrow f_\phi(\mathbf{Y})$ ▷ Round 1 with estimated PSF
- 2: $\mathbf{h}_\sigma \leftarrow \operatorname{argmin}_{\mathbf{h}_\sigma} \|\mathbf{Y} - \mathbf{X}_{\text{pre}} * \mathbf{h}_\sigma\|^2$
- 3: $\mathbf{z}_{\mathbf{Y}[1]} \leftarrow \mathbf{E}_\theta(\mathbf{Y}[1])$
- 4: $\mathbf{z}_\tau \leftarrow \text{DDIM}^{-1}(\mathbf{z}_{\mathbf{Y}[1]})$
- 5: $\mathbf{Z}_\tau \leftarrow \text{Replicate}(\mathbf{z}_\tau, N)$
- 6: **for** $t = \tau : 2$ **do**
- 7: $\hat{\mathbf{Z}}_t \leftarrow (\mathbf{Z}_t - \sqrt{1 - \bar{\alpha}_t} \mathcal{E}_\theta^{(t)}(\mathbf{Z}_t)) / \sqrt{\bar{\alpha}_t}$
- 8: $\hat{\mathbf{X}}_t \leftarrow \mathbf{D}_\theta(\hat{\mathbf{Z}}_t)$
- 9: $\bar{\mathbf{X}}_t := \operatorname{argmin}_{\mathbf{X} \in \hat{\mathbf{X}}_t + \mathcal{K}_t} \|\mathbf{Y} - \mathbf{X} * \mathbf{h}_\sigma\|^2$
- 10: $\bar{\mathbf{X}}_t \leftarrow \bar{\mathbf{X}}_t * \mathbf{h}_{\sigma_t}$
- 11: $\bar{\mathbf{Z}}_t = \mathbf{E}_\theta(\bar{\mathbf{X}}_t)$
- 12: $\mathbf{Z}_{t-1} = \sqrt{\bar{\alpha}_{t-1}} \bar{\mathbf{Z}}_t + \sqrt{1 - \bar{\alpha}_{t-1}} \mathcal{E}_t$
- 13: **end for**
- 14: $\mathbf{Z}_0 \leftarrow (\mathbf{Z}_1 - \sqrt{1 - \bar{\alpha}_1} \mathcal{E}_\theta^{(1)}(\mathbf{Z}_1)) / \sqrt{\bar{\alpha}_1}$
- 15: $\mathbf{h}_\sigma \leftarrow \operatorname{argmin}_{\mathbf{h}_\sigma} \|\mathbf{Y} - \mathbf{D}_\theta(\mathbf{Z}_0) * \mathbf{h}_\sigma\|^2$ ▷ Round 2 with refined PSF
- 16: **for** $t = \tau : 2$ **do**
- 17: $\hat{\mathbf{Z}}_t \leftarrow (\mathbf{Z}_t - \sqrt{1 - \bar{\alpha}_t} \mathcal{E}_\theta^{(t)}(\mathbf{Z}_t)) / \sqrt{\bar{\alpha}_t}$
- 18: $\hat{\mathbf{X}}_t \leftarrow \mathbf{D}_\theta(\hat{\mathbf{Z}}_t)$
- 19: $\bar{\mathbf{X}}_t := \operatorname{argmin}_{\mathbf{X} \in \hat{\mathbf{X}}_t + \mathcal{K}_t} \|\mathbf{Y} - \mathbf{X} * \mathbf{h}_\sigma\|^2$
- 20: $\bar{\mathbf{X}}_t \leftarrow \bar{\mathbf{X}}_t * \mathbf{h}_{\sigma_t}$
- 21: $\bar{\mathbf{Z}}_t = \mathbf{E}_\theta(\bar{\mathbf{X}}_t)$
- 22: $\mathbf{Z}_{t-1} = \sqrt{\bar{\alpha}_{t-1}} \bar{\mathbf{Z}}_t + \sqrt{1 - \bar{\alpha}_{t-1}} \mathcal{E}_t$
- 23: **end for**
- 24: $\mathbf{Z}_0 \leftarrow (\mathbf{Z}_1 - \sqrt{1 - \bar{\alpha}_1} \mathcal{E}_\theta^{(1)}(\mathbf{Z}_1)) / \sqrt{\bar{\alpha}_1}$
- 25: **return** \mathbf{Z}_0

In the context of blind deconvolution, an intuitive strategy is to alternate between point spread function (PSF) estimation and deconvolution. Since accurately estimating the initial PSF is challenging, we first employ a lightweight video deblurring module, DeepDeblur [15], for preliminary restoration. The initial PSF is then estimated based on this pre-restored video. Using the estimated PSF, we perform a Round 1 reconstruction with our proposed method. Subsequently, the PSF is refined based on the output of this reconstruction. The refined PSF is then utilized for the final (Round 2) reconstruction, yielding an improved result.

In summary, our method incorporates a lightweight pre-restoration step to estimate the initial PSF and employs a two-round reconstruction pipeline to achieve high-quality restoration through PSF refinement. The detailed steps of



Figure 9. Qualitative comparison of video deblurring results on the GoPro test dataset [15] compared with DeepDeblur [15].

| Method (GoPro) | FVD ↓ | LPIPS ↓ | PSNR ↑ | SSIM ↑ |
|-----------------|--------------|--------------|--------------|--------------|
| DeepDeblur [15] | 0.119 | 0.116 | 30.93 | 0.904 |
| Ours (blind) | 0.020 | 0.009 | 37.55 | 0.981 |

Table 6. Quantitative evaluations on video deblurring using the GoPro test dataset [15]. **Bold** indicates the best results.

the algorithm are outlined in Algorithm 2.

The GoPro dataset comprises 240 fps videos captured using a GoPro camera, where motion blur is synthetically generated by averaging 7 to 13 consecutive frames [15]. We utilized the GoPro test dataset for our experiments and performed blind video reconstruction using Algorithm 2, where blurred inputs were created by randomly averaging 7 to 13 frames. To highlight our approach’s effectiveness, we compared our method’s reconstruction results with those obtained from the pre-restoration module. Our method significantly enhances the reconstruction quality, achieving highly satisfactory results. As demonstrated in Fig. 9 and summarized in Table 6, our proposed approach, denoted as Ours (blind), consistently outperforms the supervised base-

line [15] on the GoPro test dataset. The zoomed-in views of the signboards and billboards in Fig. 9 show that details, such as text, are recovered with greater precision using our method. This improvement highlights that incorporating a diffusion prior facilitates a more accurate estimation of the PSF. These results demonstrate the potential of our method to be extended for solving various blind inverse problems, as evidenced by this experiment.

8. Comprehensive visualizations

For an in-depth understanding of the experimental results, we provide video visualizations on our anonymous project page⁵. The page features 36 paired visualizations of measurements and reconstructions across various aspect ratios and degradation types. As shown on the project page, our method delivers highly satisfactory reconstruction results for various spatio-temporal inverse problems.

Additional comparisons with baselines are available on our supplementary anonymous project page⁶. In base-

⁵<https://vision-xl.github.io/>

⁶<https://vision-xl.github.io/supple/>

line comparisons, ADMM-TV struggles to reconstruct temporal degradations, and SVI [13] exhibits poor temporal consistency. DiffIR2VR [33] frequently fails to reconstruct and produces undesired artifacts, likely due to errors in the optical flow estimation module. In contrast, our approach achieves superior performance across various spatio-temporal inverse problems.

We also provide visualizations of ablation studies. Regarding initialization effects, our batch-consistent inversion significantly improves temporal consistency compared to random noise initialization or batch-consistent noise initialization [13]. Regarding the low-pass filter effect, we observe that applying a well-scheduled low-pass filter produces cleaner results with fewer artifacts. Without the low-pass filter, artifacts such as the grid pattern under the red bridge or the lattice-like texture on the body of the sea snake are noticeable.

We strongly encourage you to visit these project pages to explore the superior reconstruction performance of our method.